Subsurface Sensing Technologies and Applications Vol. 4, No. 4, October 2003 (©2003)

An Object-Based Contrast Source Inversion Method for Homogeneous Targets

Haihua Feng,[1] Vincenzo Galdi,[1,2] and David A. Castañon[1,*]

[1] Department of Electrical & Computer Engineering, Boston University, 8 Saint Mary's Street, Boston, MA 02215, USA
[2] Waves Group, Department of Engineering, University of Sannio Palazzo Dell'Aquila Bosco Lucarelli, Corso Garibaldi 107, I-82100 Benevento, Italy

Received August 16 2002; revised May 15 2003

An object-based inverse scattering algorithm is presented for electromagnetic imaging of homogeneous dielectric targets in a lossless, homogeneous background. The proposed approach embodies the use of a contrast source inversion method in conjunction with a curve-evolution-based reconstruction technique, thereby integrating the attractive computational features of the former with the robustness and edge-preserving capabilities of the latter. Numerical results involving single- and double-target configurations are presented to validate the approach and demonstrate its capabilities.

Key Words. Inverse scattering, contrast source inversion, ground-penetrating radar, subsurface imaging.

1. Introduction

Electromagnetic (EM) imaging of penetrable objects embedded in complex environments is a topic of paramount interest in a variety of disciplines, with potential applications including bio-medical imaging, non-destructive testing, humanitarian demining, etc. In these applications, one is interested in reconstructing, from scattered field observations, the electrical properties (e.g., permittivity and conductivity) of a suitable test region, in order to detect, localize and classify possible anomalies. Most of the challenges involved in this inverse scattering scenario stem from its inherent

*To whom all correspondence should be addressed. Phone: 617-353-9880; fax: 617-353-6440; e-mail: dac@bu.edu

1566-0184/03/1000-0355/0

ill-posedness [1], which affects the numerical conditioning of the inversion algorithms, i.e., their sensitivity to noise and data uncertainty. A common approach to cope with this limitations is based on the use of regularization techniques which tend to restrict the solution space via exploitation of suitable a priori information [2]. Another key issue is related to the intrinsic *nonlinearity* of the model, which complicates significantly the inversion procedure, due to the existence of possible *false solutions* (see, e.g., [3] and the references therein). Although significant advances have been achieved during the past decade (see, e.g., [2–5] for a comprehensive review), devising effective imaging techniques is still a worthwhile task, which requires clever blend of EM modeling and advanced signal processing in order to grant physical insight into the problem and to exploit possible a priori information in the most fruitful way.

In this connection, *object-based* (OB) inversion techniques are rapidly emerging as an attractive alternative to traditional *pixel-based* approaches. The key idea behind OB techniques is to focus on robust *global* features of the target (e.g., shape, contrast, etc.), instead of trying to image it *pointwise*. Besides mitigating the ill-posedness of the problem, this typically yields better estimation of key features of the target image (such as *edges*) which is highly desirable in localization/classification procedures. OB inversion techniques use simple parameterizations of objects in terms of nearly homogeneous regions delineated by boundaries, and use variational techniques to search for optimal location of boundaries and contrast values. Similar variational techniques are used extensively in the computer vision literature for segmentation problems, and are based on the work of Mumford and Shah [7]. The Mumford–Shah framework has been combined with curve evolution techniques recently [8,9] to obtain fast OB algorithms for object segmentation in computer vision.

In this paper, we describe an OB algorithm for reconstructing two-dimensional (2-D) homogeneous dielectric targets in a homogeneous background medium (free space). The proposed approach combines the contrast source inversion (CSI) method in [6] with a popular OB technique, based on *curve-evolution* algorithms [8–11]. The basic idea is to integrate the proven versatility and computational efficiency of the CSI method with the desirable robustness and edge-preserving capabilities of OB reconstruction techniques.

The remainder of the paper is organized as follows. In Section 2, the problem formulation is outlined and the background theory on CSI methods is briefly reviewed, with definition of the notation used throughout the paper. In Section 3, the proposed OB-CSI method is described, and the various algorithmic steps and tasks involved are detailed. Representative numerical results involving single- and double-target geometries are presented and discussed in Section 4. Conclusions follow in Section 5.

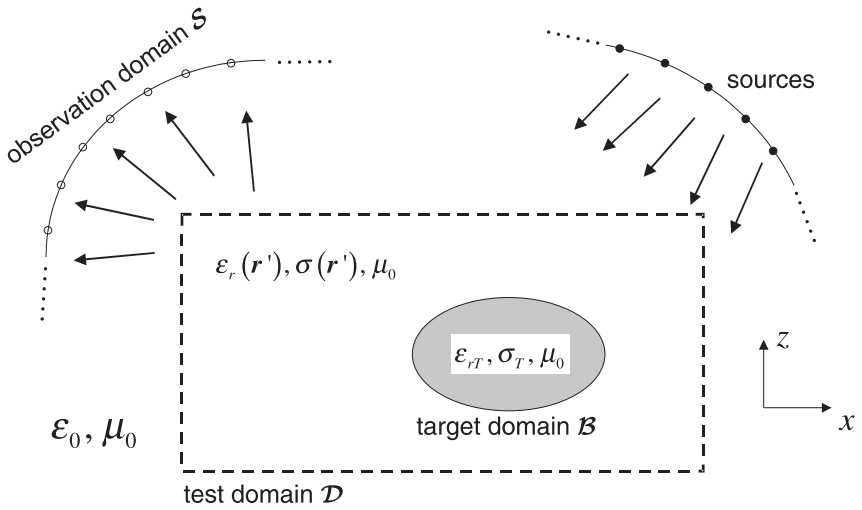

Figure 1. Problem geometry. A homogeneous target with relative electric permittivity ε_{rT} and electrical conductivity σ_T occupies the region $\mathcal{B}$ (target domain), lying inside a test domain $\mathcal{D}$, in free space. A single-frequency, time-harmonic, TM-polarized illumination is generated via an array of N_s line-sources. The backscattered field is observed at N_r fixed receiver locations (observation domain).

2. Problem Formulation and Background Theory

The problem geometry is illustrated in Figure 1, which shows a scattering object (target) occupying a domain $\mathcal{B}$ (target domain) in a homogeneous lossless background medium. Here, the background medium is assumed to be free space, with dielectric permittivity and magnetic permeability denoted as ε_0 and μ_0, respectively. The target is assumed to be homogeneous and nonmagnetic ($\mu = \mu_0$); its location, relative dielectric permittivity ε_{rT} and electric conductivity σ_T are *unknown*. However, the (possibly multiply-connected) target domain $\mathcal{B}$ is assumed to lie within a known (larger, simply connected) domain $\mathcal{D}$ (test domain). In what follows, we consider a two-dimensional (2-D) formulation in a (x, z) coordinate system, with all fields and geometries implicitly assumed to be y-independent. Moreover, we assume a multistatic transmitter/receiver configuration with suppressed $\exp(-i\omega t)$ time dependence. Specifically, we assume a transverse magnetic (TM) illumination generated by an array of N_s line sources, restricting our attention to the y-directed electric field $E(x, z)$ from which all other field quantities of interest can be computed via Maxwell's equations. The complex (magnitude and phase) field scattered by the object is observed at a number N_r of receiver locations lying on the curve $\mathcal{S}$ (observation domain). Both source and

observation domains are assumed to lie outside the test domain $\mathscr{D}$. The actual goal of this investigation is the *imaging* of the test domain $\mathscr{D}$ in Figure 1, i.e., the reconstruction, from scattered field observations, of its electrical properties ε_r and σ, in order to detect, localize and possibly classify the embedded target(s).

The following three subsections (2.1–2.3) are intended as an introduction to the CSI method and to the notation used throughout the paper; the background theory presented does not contain original material, and can thus be skipped by the more expert reader.

2.1. Forward Scattering Formulation

The total field E_j in the test domain $\mathscr{D}$, due to an incident field E_j^{inc} generated by the j-th line-source transmitter, $j = 1, \ldots, N_s$, is ruled by the well-known Lippman–Schwinger integral equation [12],

$$E_j(\mathbf{r}) = E_j^{inc}(\mathbf{r}) + k_0^2 \int_{\mathscr{D}} G(\mathbf{r}, \mathbf{r}'; k_0)\chi(\mathbf{r}')E_j(\mathbf{r}')\, d\mathbf{r}', \quad \mathbf{r} \in \mathscr{D} \tag{1}$$

where $\mathbf{r} \equiv (x, z)$ and $\mathbf{r}' \equiv (x', z')$ denote points in $\mathscr{D}$, and $k_0 = \omega\sqrt{\varepsilon_0\mu_0} = 2\pi/\lambda_0$ is the free-space wavenumber, with λ_0 denoting the free-space wavelength. Moreover,

$$G(\mathbf{r}, \mathbf{r}'; k_0) = \frac{i}{4} \mathrm{H}_0^{(1)}(k_0|\mathbf{r} - \mathbf{r}'|) \tag{2}$$

is the 2-D free-space Green's function, with $\mathrm{H}_0^{(1)}$ denoting the zero-th order Hankel function of the first kind [13], and

$$\chi(\mathbf{r}') = \chi^r(\mathbf{r}') + i\chi^i(\mathbf{r}') = \varepsilon_r(\mathbf{r}') - 1 + i\frac{\sigma(\mathbf{r}')}{\omega\varepsilon_0} \tag{3}$$

is the contrast function, also referred to as *object function*. Similarly, the scattered field F_j observed at receiver location $\mathbf{r}$, due to the same incident field E_j^{inc}, is given by [12]

$$F_j(\mathbf{r}) = k_0^2 \int_{\mathscr{D}} G(\mathbf{r}, \mathbf{r}'; k_0)\chi(\mathbf{r}')E_j(\mathbf{r}')\, d\mathbf{r}', \quad \mathbf{r} \in \mathscr{S} \tag{4}$$

Equations (1) and (4) are usually referred to as *object* and *data equations*, respectively. Following [6], we rewrite them in a compact symbolic form as

$$E_j = E_j^{inc} + G_D\chi E_j, \quad \mathbf{r} \in \mathscr{D} \tag{5}$$

$$F_j = G_S\chi E_j, \quad \mathbf{r} \in \mathscr{S} \tag{6}$$

with G_D and G_S denoting the integral operators in (1) and (4), respectively. These operators are actually *identical*, and the different subscripts D and S

are used only to highlight the different location of the observation point **r** (in $\mathscr{D}$ and $\mathscr{S}$, respectively).

It is instructive to combine object and data equations, (5) and (6), as

$$F_j = G_S[\chi(I - G_D\chi)^{-1}E_j^{inc}] \tag{7}$$

where I denotes the identity operator, and the superscript -1 indicates a *formal* inverse. From (7), the intrinsic nonlinearity of the inverse scattering problem with respect to the object function χ emerges clearly. Starting from the fully nonlinear exact formulation in (7), a variety of approximation schemes have been proposed to invert the forward scattering model in a reliable and computationally feasible fashion. Prominent among them are the linearized methods based on Born-type approximations. Starting from the simplest, and crudest, Born approximation ($G_D = 0$ in (7)), which linearizes the model in the weak scattering (i.e., weak contrast, $|\chi| \ll 1$) limit, more sophisticated *iterative* [14], and *distorted* [15] alternatives have been proposed to cope with higher-contrast targets. Nonlinear approaches, based on the so-called "extended" Born approximation [16] have also been explored.

2.2. Contrast Source Formulation

Since, as seen from (5)–(7), the nonlinearity of the problem arises from the occurring of the object function and the total field as a *product*, it is suggestive to re-formulate the problem introducing the quantities

$$W_j = \chi E_j \tag{8}$$

It is readily verified that the fields E_j satisfy the equation

$$(\nabla_t^2 + k_0^2)E_j = -k_0^2 W_j \quad \text{in } \mathscr{B} \tag{9}$$

with ∇_t^2 denoting the transverse Laplace operator. Because of (9), W_j are usually referred to as *contrast sources*. The object equations in (5) are accordingly rewritten as

$$E_j = E_j^{inc} + G_D W_j \tag{10}$$

or equivalently, using (8),

$$\chi E_j^{inc} = W_j - \chi G_D W_j \tag{11}$$

whereas the data equations in (6) become

$$F_j = G_S W_j \tag{12}$$

2.3. Contrast Source Inversion

Equation (12) represents a classic ill-posed problem of longstanding interest. The reader is referred to [6,17–21] and the references therein for a

comprehensive overview. In particular, it has been shown that standard inversion techniques (e.g., conjugate gradient) can lead to *unphysical* solutions. To overcome this problem, more sophisticated inversion techniques have been devised (see, e.g., [6,22,23]). In what follows, we focus on the approach proposed in [6], which has been proven to be particularly versatile and effective. Following [6], we define the cost functional

$$J(\chi, \underline{W}) = \alpha_1 \sum_{j=1}^{N_s} \|F_j - G_S W_j\|_{\mathscr{S}}^2 + \alpha_2 \sum_{j=1}^{N_s} \|\chi E_j^{inc} - W_j + \chi G_D W_j\|_{\mathscr{D}}^2 + \beta J_{REG}(\chi, \underline{W}) \tag{13}$$

and formalize the inverse scattering problem as finding the object function χ and the contrast sources $\underline{W} = \{W_j\}_{j=1,\ldots,N_s}$ which minimize it. In (13), the first two terms encourage *data fidelity*, by measuring the error in the data and object equations in (12) and (11), respectively, with $\|\cdot\|_{\mathscr{S}}^2$ and $\|\cdot\|_{\mathscr{D}}^2$ denoting L_2 norms defined in $\mathscr{S}$ and $\mathscr{D}$, respectively, and with α_1 and α_2 being suitable normalization coefficients. In what follows, we shall use

$$\alpha_1^{-1} \equiv \sum_{j=1}^{N_s} \|F_j\|_{\mathscr{S}}^2, \quad \alpha_2^{-1} \equiv \sum_{j=1}^{N_s} \|E_j^{inc}\|_{\mathscr{D}}^2 \tag{14}$$

The original contrast source inversion technique uses a different normalization coefficient

$$\alpha_2^{-1} \equiv \sum_{j=1}^{N_s} \|\chi E_j^{inc}\|_{\mathscr{D}}^2$$

which introduces an additional iteration in the algorithm. In order to keep the exposition simple, we use the normalizations in Eq. (14). It is straightforward to extend our algorithm to the normalization of Eq. (15) by using an iteration dependent normalization that uses a previous estimate of χ in Eq. (15), as in [6].

The third term in (13), J_{REG}, is a *regularization* term which helps restoring well-posedness of the problem [1] via exploitation of suitable a priori information about geometrical and constitutive features (e.g., smoothness, homogeneity) of the target. The proper choice of the regularization parameter β is an important issue, for which a number strategies have been proposed (see, e.g., [24]). In this connection, alternative regularization schemes based, e.g., on *multiplicative* constraints have also been proposed [25–27].

3. Object-Based Contrast Source Inversion

3.1. Preliminary Considerations

Object-based (OB) inversion techniques have been widely investigated in image processing, with many important applications in problems such as object boundary detection and image segmentation. OB approaches typically rely on parametric or semi-parametric deformable shape models for the object function which incorporate possible a priori information about geometrical and constitutive properties of the target, focusing on its *robust* features. For our specific problem, involving *homogeneous* targets, it is suggestive to estimate the key features of the target (e.g., shape and contrast) *directly* rather than trying to retrieve them *pointwise*, thereby avoiding the inherent problems of a posteriori edge detection. In this connection, OB techniques offer an attractive alternative to standard pixel-based imaging techniques from both the computational and reconstruction quality viewpoints. In the last few years, several applications of OB approaches to EM inverse scattering problems have been explored. For instance, in [28], a shape-based approach has been applied in conjunction with the Newton–Kantorovich technique to inverse scattering of conducting cylinders buried in a homogeneous halfspace. For the same problem, but for dielectric targets, an *effective* scattering model based on circular cylinders, with radius, permittivity and center position to be retrieved, has been proposed in [29]. Applications to *inhomogeneous* backgrounds/targets have been explored in [30], via the use of low-order polynomial expansions for background and target permittivity and quadratic B-spline parameterizations for the target boundary. A noteworthy class of OB inversion techniques is represented by *curve evolution* (CE) techniques (see, e.g., [8–11]), where a *gradient flow* is designed which attracts initial closed curves to the target boundary. Such techniques have been explored in [31–34] in connection with nonlinear inverse scattering problems involving penetrable targets with *known* electric properties. More recently, applications to underground imaging of shallowly-buried low-contrast targets in the presence of flat and moderately rough air-soil interfaces have also been given attention [35–38].

3.2. Proposed Approach

As stated previously, our approach is based on the combined use of OB reconstruction techniques and CSI. To this end, the target is parameterized via a semiparametric deformable-shape model, and the cost functional in (13) is modified accordingly and subsequently minimized using a coordinate descent (alternating minimization) method [39]. The various algorithmic steps are detailed below.

3.2.1. Object Parameterization and Problem Formulation

Although, in principle, the method can handle multiple targets, here we focus on the simplest scenario in Figure 1, where a single homogeneous target with relative permittivity ε_{rT} and electrical conductivity σ_T occupies the region $\mathscr{B}$ bounded by a continuous curve $\vec{C}$. The object function can thus be parameterized as

$$\chi(\mathbf{r}) = \hat{\chi}\Pi_{\mathscr{B}}(\mathbf{r}), \quad \hat{\chi} = \hat{\chi}^r + i\hat{\chi}^i \tag{16}$$

with $\hat{\chi}^r = \varepsilon_{rT} - 1$ and $\hat{\chi}^i = \sigma_T/(\omega\varepsilon_0)$. Here and henceforth, the superscripts r and i denote the real and imaginary part, respectively. Moreover, $\Pi_{\mathscr{B}}$ represents the characteristic function of the target region $\mathscr{B}$,

$$\Pi_{\mathscr{B}}(\mathbf{r}) = \begin{cases} 1, & \mathbf{r} \in \mathscr{B} \\ 0, & \mathbf{r} \notin \mathscr{B} \end{cases} \tag{17}$$

The inverse scattering problem is thereby reduced to estimating the target boundary $\vec{C}$ and the single value of contrast $\hat{\chi}$. In view of the chosen parameterization (16) for the object function, we rewrite the cost functional in (13) as

$$\begin{aligned} J(\hat{\chi}, \vec{C}; \underline{W}) &= \alpha_1 \sum_{j=1}^{N_s} \|F_j - G_S W_j\|_{\mathscr{S}}^2 + \alpha_2 \sum_{j=1}^{N_s} \|\hat{\chi} E_j - W_j\|_{\mathscr{B}(\vec{C})}^2 + \gamma \int_{\vec{C}} d\ell \\ &= \alpha_1 \sum_{j=1}^{N_s} \|F_j - G_S W_j\|_{\mathscr{S}}^2 + \alpha_2 \sum_{j=1}^{N_s} |\hat{\chi}\overline{E}_j - \overline{W}_j|^2 + \gamma \int_{\vec{C}} d\ell \end{aligned} \tag{18}$$

where $\mathscr{B}(\vec{C})$ denotes the region bounded by the closed curve $\vec{C}$, and

$$\overline{E}_j = \int_{\mathscr{B}(\vec{C})} E_j(\mathbf{r}')\, d\mathbf{r}', \quad \overline{W}_j = \int_{\mathscr{B}(\vec{C})} W_j(\mathbf{r}')\, d\mathbf{r}' \tag{19}$$

with E_j being defined in (10). In the second term of the modified cost functional in (18), we have enforced the homogeneity condition in (16), which can be viewed as prior-information-based *implicit* regularization. Additional regularization is provided by the third term in (18), by penalizing the arc-length of the estimated curve, with the choice of the regularization parameter γ affecting its smoothness. This term is motivated by the Mumford–Shah approach [7] and serves as a regularization on target shape. In our implementation, γ is empirically selected by trial and error, taking into account prior expectations about target geometry (e.g., size and smoothness).

The proposed algorithm is based on a simple coordinate descent method [39], involving the alternating minimization of the cost functionals $J_{\hat{\chi},\vec{C}}(\underline{W})$ and $J_{\underline{W}}(\hat{\chi}, \vec{C})$ obtained from (18) by fixing the contrast sources W_j

and the OB-parameterized object function $(\hat{\chi}, \vec{C})$, respectively, i.e.,

$$J_{\hat{\chi},\vec{C}}(\underline{W}) = \alpha_1 \sum_{j=1}^{N_s} \|F_j - G_S W_j\|^2_{\mathscr{S}} + \alpha_2 \sum_{j=1}^{N_s} \|\hat{\chi} E_j - W_j\|^2_{\mathscr{B}(\vec{C})} \tag{20}$$

$$J_{\underline{W}}(\hat{\chi}, \vec{C}) = \frac{1}{2} \sum_{j=1}^{N_s} |\hat{\chi}\overline{E}_j - \overline{W}_j|^2 + \gamma \int_{\vec{C}} d\ell \tag{21}$$

It is readily recognized that, for fixed $(\hat{\chi}, \vec{C})$, (20) is a *quadratic* functional, and therefore its minimization does not pose particular challenges. In our implementation, this minimization is carried out via standard conjugate gradient (CG) optimization algorithms [40], in a suitably discretized test domain. Conversely, the cost functional in (21), for fixed $\underline{W}$, is *nonquadratic* (due to the presence of the arc-length regularization term) and involves an OB-parameterized object function.[1] In our implementation, its minimization is performed via a *curve-evolution* (CE) technique, as detailed in subsection 3.2.2.

A schematic flow-chart of the end-to-end approach is shown in Figure 2. The core of the approach consists of the alternating minimization of the cost functionals (20) (via standard CG algorithms [40]) and (21) (via CE algorithms), as described above. Concerning the initialization step, it is clear that one needs an initial estimate of the object function or of the inverse sources. Among the various strategies that we have explored (including, e.g.,

[1]Note that a notationally more convenient scaling in the regularization parameters has been introduced in (21).

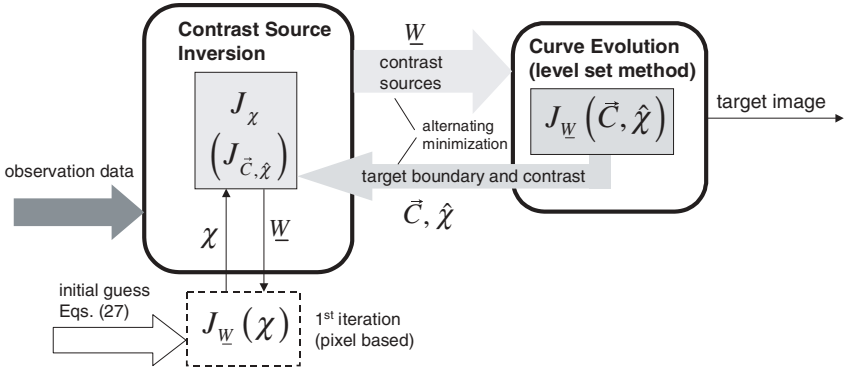

Figure 2. Schematic flow-chart of the proposed object-based contrast source inversion approach.

the exploitation of Born-approximated solutions), the most robust and reliable is based on a preliminary pixel-based CSI estimation. This strategy is described in subsection 3.2.3.

We highlight that the proposed OB-CSI approach differs substantially from traditional CE approaches to nonlinear inverse scattering such as, e.g., [31–34]. These approaches are usually based on adjoint-field computation, and are typically restricted to *known-contrast* targets. Conversely, our approach relies on the proven computational efficiency of the CSI method, and allows for *simultaneous* estimation of *both* target shape *and* contrast.

3.2.2. Curve Evolution

As stated previously, the cost functional in (21), for fixed $\underline{W}$, is minimized via a CE approach. As typical in CE techniques, this is accomplished by designing a gradient flow that attracts an initial closed curve to the boundary of the target region $\mathscr{B}$. Given a family of smooth curves $\vec{C}(\tau)$ parameterized by τ, we search for the curve in this family and the contrast value $\hat{\chi}$ that minimize the cost functional in (21). For a given curve $\vec{C}(\tau)$, by enforcing the stationarity of (21) with respect to the contrast $\hat{\chi}$, the following equations are obtained

$$\frac{\partial}{\partial \hat{\chi}^r} J_{\underline{W}}(\tau, \hat{\chi}) = 0 \quad \text{and} \quad \frac{\partial}{\partial \hat{\chi}^i} J_{\underline{W}}(\tau, \hat{\chi}) = 0 \tag{22}$$

By combining (21) and (22), one obtains a couple of linear equations that must be satisfied by the real and imaginary parts of the contrast $\hat{\chi}$,

$$\begin{cases} \sum_{j=1}^{N_s} (\overline{W}_j^r - \hat{\chi}^r \overline{E}_j^r + \hat{\chi}^i \overline{E}_j^i) \overline{E}_j^r + (\overline{W}_j^i - \hat{\chi}^i \overline{E}_j^r - \hat{\chi}^r \overline{E}_j^i) \overline{E}_j^i = 0 \\ \sum_{j=1}^{N_s} (\overline{W}_j^r - \hat{\chi}^r \overline{E}_j^r + \hat{\chi}^i \overline{E}_j^i) \overline{E}_j^i - (\overline{W}_j^i - \hat{\chi}^i \overline{E}_j^r - \hat{\chi}^r \overline{E}_j^i) \overline{E}_j^r = 0 \end{cases} \tag{23}$$

To minimize the cost functional in (21), the curve $\vec{C}(\tau)$ is evolved along the direction of steepest descent, i.e., along the negative gradient of $J_{\underline{W}}$ with respect to $\vec{C}(\tau)$. Proceeding as in [35,36], one finds

$$\begin{aligned} \frac{d\vec{C}}{d\tau} = -\nabla_\tau J_{\underline{W}}(\tau, \hat{\chi}) = \sum_{j=1}^{N_s} \{ & (\overline{W}_j^r - \hat{\chi}^r \overline{E}_j^r + \hat{\chi}^i \overline{E}_j^i)[\hat{\chi}^r E_j^r(\mathbf{r}_c') - \hat{\chi}^i E_j^i(\mathbf{r}_c')] \mathbf{n}_c \\ & + (\overline{W}_j^i - \hat{\chi}^i \overline{E}_j^r - \hat{\chi}^r \overline{E}_j^i)[\hat{\chi}^i E_j^r(\mathbf{r}_c') + \hat{\chi}^r E_j^i(\mathbf{r}_c')] \mathbf{n}_c \} + \gamma \kappa_c \mathbf{n}_c \end{aligned} \tag{24}$$

where $J_{\underline{W}}(\tau, \hat{\chi}) \equiv J_{\underline{W}}[\vec{C}(\tau), \hat{\chi}]$, E_j and $\bar{E}_j$ are defined in (10) and (19), respectively, $\mathbf{r}_c'$ denotes a point on the curve $\vec{C}(\tau)$, and $\mathbf{n}_c$ and κ_c indicate the outward normal and the signed curvature of the curve at $\mathbf{r}_c'$, respectively [35,36].

For numerical implementation, the evolution in (24) needs to be discretized in τ and stepped forward. The procedure is initialized through a rough initial guess of the target boundary, which is subsequently used to obtain, via (23), the initial contrast estimate. The procedure is thus evolved, with alternative updating of the curve $\vec{C}(\tau)$ (via (24)) and of the contrast estimate $\hat{\chi}$ (via (23)) until convergence is achieved. In this connection, the target boundary initial guess was found to be not particularly critical for the overall accuracy, affecting primarily the convergence rate. Our numerical implementation is based on the level set method [31,32,41], which was found to yield numerically efficient and stable evolution. Implementation details are similar to those in [35,36] and therefore are not discussed here.

3.2.3. Pixel-Based CSI Initialization

As discussed in subsection 3.2.1, the initialization procedure in our approach is based on a preliminary pixel-based CSI estimation. To this end, the test domain $\mathscr{D}$ is discretized in a number N_p of suitably small pixels. The proposed procedure, close in spirit to that in [6], is aimed at minimizing the CSI cost functional in (13), with a *total variation* regularization term [42]

$$J_{reg}(\chi) = \|D\chi\|_{\mathscr{D}}^{1} \equiv \sum_{p=1}^{N_p} \sqrt{|(D_x\chi)_p|^2 + |(D_z\chi)_p|^2} \tag{25}$$

where D_x and D_z denote finite differences operators in the x and z direction, respectively. This regularization term encourages the expected piecewise smoothness in the reconstructed object function and contrast sources, by penalizing the L_1 norm of the spatial gradient operator D. However, as compared with the L_2 norm in the standard Tikhonov regularization [1], the L_1 gradient penalty in (25) is less penalizing on *large* jumps, thus allowing sharper edges to form in the reconstructed object function and yielding less blurred reconstructions. Also in this case, we use an alternating minimization scheme involving the cost functionals

$$J_{\underline{W}}(\chi) = \alpha_2 \sum_{j=1}^{N_s} \|\chi E_j - W_j\|_{\mathscr{D}}^2 + \beta J_{reg}(\chi) \tag{26}$$

$$J_{\chi}(\underline{W}) = \alpha_1 \sum_{j=1}^{N_s} \|F_j - G_S W_j\|_{\mathscr{S}}^2 + \alpha_2 \sum_{j=1}^{N_s} \|\chi E_j - W_j\|_{\mathscr{D}}^2 \tag{27}$$

obtained from (13) by fixing the contrast sources $\underline{W}$ and the object function χ, respectively, and with E_j defined in (19). Again, it is recognized that (27) is a *quadratic* functional, whereas (26) is *nonquadratic* due to the presence of the

L_1 regularization term. The procedure is initialized by solving two linear problems, obtained from (26) (with $\beta = 0$) and (27) (with $\alpha_2 = 0$), which yield the rough initial estimates for the contrast sources and the object function, respectively,

$$W_j^{(0)} = G_S^{\dagger} F_j, \quad \chi^{(0)} = P^{(0)\dagger} Q^{(0)} \tag{28}$$

with

$$P^{(0)} \equiv \sum_{j=1}^{N_s} E_j^{(0)}, \quad Q^{(0)} \equiv \sum_{j=1}^{N_s} W_j^{(0)} \tag{29}$$

In (28), the subscript † indicates the pseudo-inverse operator,

$$A^{\dagger} \equiv (A^T A)^{-1} A^T \tag{30}$$

with T denoting the complex conjugate transpose operator. The procedure is then evolved with alternating minimizations of the functionals in (26) and (27). Minimization of the (quadratic) cost functional in (27) is accomplished via standard CG algorithms [40], whereas minimization of (26) is slightly more involved. In this connection, we use an iterative scheme based on *half-quadratic* approximations [42]. At the n-th alternating minimization step, the estimates of the contrast sources W_j are obtained by solving the linear problem

$$(\alpha_1 G_S^T G_S + \alpha_2 R^{(n)T} R^{(n)}) W_j^{(n)} = \alpha_1 G_S^T F_j + \alpha_2 R^{(n)T} \chi^{(n-1)} E_j^{inc} \tag{31}$$

where $R^{(n)} = \chi^{(n-1)} G_D - I$. Once the $W_j^{(n)}$ are computed, the estimate of the object function, $\chi^{(n)}$, is obtained via an iterative procedure, involving solution of a sequence of N_l linear problems [42]

$$[\alpha_2 P^{(n)T} P^{(n)} + \beta (D_x^T \Lambda^{(n,l)} D_x + D_z^T \Lambda^{(n,l)} D_z)] \chi^{(n,l)} = \alpha_2 P^{(n)T} Q^{(n)},$$
$$l = 1, \ldots, N_l \tag{32}$$

where

$$P^{(n)} = \sum_{j=1}^{N_s} E_j^{(n)}, \quad Q^{(n)} = \sum_{j=1}^{N_s} W_j^{(n)} \tag{33}$$

$$\Lambda^{(n,l)} = \operatorname{diag}\left\{ \left[\left| (D_x \chi^{(n-1,l)})_p \right|^2 + \left| (D_z \chi^{(n-1,l)})_p \right|^2 + \eta^2 \right]^{-1/2} \right\},$$
$$p = 1, \ldots, N_p \tag{34}$$

In (34), η is a small smoothing parameter which controls the closeness to the true L_1 norm solution and the convergence speed [42]. The estimate of the

object function at the n-th alternating minimization step is thus given by $\chi^{(n)} = \chi^{(n, N_I)}$. The sought initial estimate of the contrast sources W_j is obtained via M alternating minimization iterations as in (31)–(34). We emphasize that this estimate does not need to be very accurate, and therefore it is not necessary to reach *full* convergence in the alternating minimization scheme (31)–(34).

4. Numerical Results

In order to validate and calibrate the proposed OB-CSI approach, an extensive series of numerical experiments was performed. In all numerical simulations presented below, the *measured* fields were synthetically generated via full-wave solution of the forward scattering problem, using the multifilament current method in [43]. To begin with, we consider a single-target configuration involving an elliptic cylinder with center at $(x_0, z_0) = (0, 0)$, radii $R_x = 0.5\lambda_0$ and $R_z = 0.25\lambda_0$, and contrast $\chi = 1 + i0.5$. For this example, $N_s = 30$ line sources and $N_r = 30$ receivers were assumed, evenly spaced on a circle of radius $R_0 = 1.5\lambda_0$ centered at (0, 0). The test domain $\mathscr{D}$ to be imaged was chosen as a $2.4\lambda_0 \times 2.4\ \lambda_0$ square surrounding the target, discretized into $N_p = 30 \times 30$ pixels. We used two complete iterations (plus the pixel-based initialization) of the OB-CSI reconstruction algorithm in subsection 3.2.

Reconstruction results are compared with the *ground truth* in Figure 3. Figures 3a and d show the actual contrast (real and imaginary parts, respectively), whereas Figures 3b and e show the corresponding pixel-based CSI initial estimates obtained after $M = 128$ iterations (subsection 3.2.3); these reconstructions resemble those in [6]. The final OB-CSI reconstruction results, obtained after two complete iterations of the algorithm in subsection 3.2, are shown in Figures 3c and f, with CE and regularization parameters indicated in the figure captions. Good accuracy is observed in both target boundary and contrast estimation (estimated value: $\hat{\chi} = 0.93 + i0.47$). The boundary estimation capabilities of the proposed approach are highlighted in Figure 4, which shows the actual target boundary overlayed on the OB-CSI final estimation. No particular reconstruction improvement was observed by using more than two complete iterations of the algorithm. Next, in order to assess the reliability of the algorithm, we performed a number of sensitivity tests with respect to possible pollution in the observed data. For the same target as in Figures 3 and 4, typical reconstruction results obtained by using observation data corrupted by uniform noise ($\pm 10\%$ in magnitude, $\pm 10^o$ in phase) are shown in Figure 5. The OB-CSI algorithm turns out to be remarkably robust, with the reconstruction results being only slightly worse. As a more challenging example, we consider a double-target configuration,

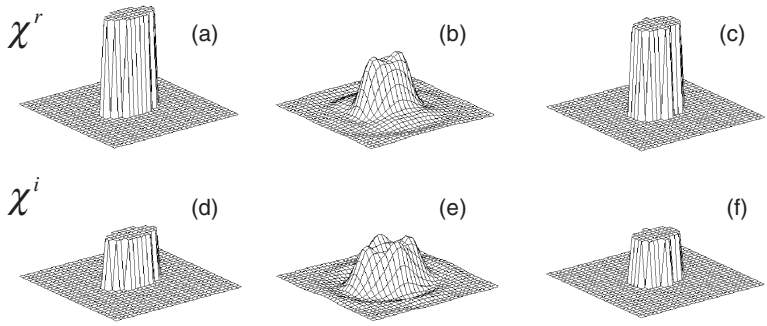

Figure 3. Single-target configuration: reconstruction examples. Target: elliptic cylinder with center at $(x_0, z_0) = (0, 0)$, radii $R_x = 0.5\lambda_0$ and $R_z = 0.25\lambda_0$, and contrast $\chi = 1 + i0.5$. Sources and receivers: $N_s = 30$ line sources and $N_r = 30$ receivers were assumed, evenly spaced on a circle of radius $R_0 = 1.5\lambda_0$ centered at (0, 0). Test domain: $2.4 \times 2.4\lambda_0$ square surrounding the target, discretized into $N_p = 30 \times 30$ pixels. (a), (d) Ground truth (real and imaginary contrast, respectively). (b), (e) Pixel-based CSI initial estimate (subsection 3.2.3) after $M = 128$ iterations with $N_I = 10$ and $\beta = 10^{-4}$. (c), (f) Final OB-CSI reconstruction via two iterations of the algorithm in subsection 3.2. CE parameters: 250 τ-steps with $\gamma = 0.1$ plus 200 steps with $\gamma = 0.03$ (1st iteration), 150 steps with $\gamma = 0.015$ (2nd iteration); estimated contrast: $\hat{\chi} = 0.93 + i0.47$.

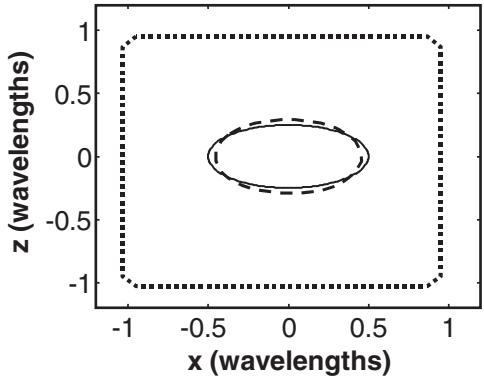

Figure 4. Parameters as in Figure 3. Actual target boundary overlayed on OB-CSI final estimation. —— Actual target boundary; – – – Estimated target boundary; · · · CE initial conditions.

starting with the case where the two targets have the same contrast. Specifically, we assume

- Target 1: Elliptic cylinder centered at $(x_{01}, z_{01}) = (-0.5\lambda_0, 0)$ with radii: $R_{x1} = 0.5\lambda_0$, $R_{z1} = 0.25\lambda_0$,
- Target 2: Elliptic cylinder centered at $(x_{02}, z_{02}) = (0.5\lambda_0, 0)$ with radii: $R_{x2} = 0.25\lambda_0$, $R_{z2} = 0.5\lambda_0$,

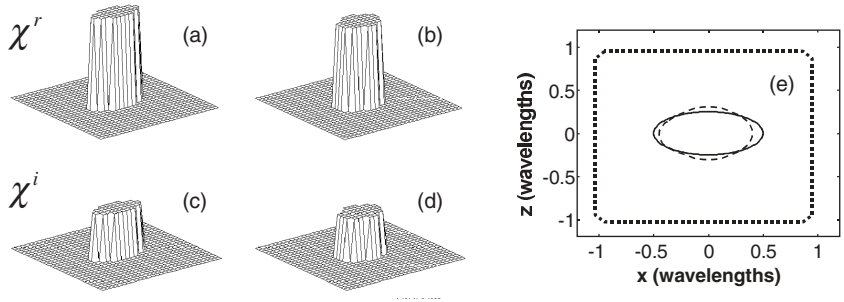

Figure 5. Parameters as in Figure 3, but for observation data corrupted by uniform noise (±10% in magnitude, $\pm 10^o$ in phase). (a), (c) Ground truth (real and imaginary contrast, respectively). (b), (d) Final OB-CSI reconstruction via two iterations of the algorithm in subsection 3.2. CE parameters as in Figure 3; estimated contrast: $\hat{\chi} = 0.91 + i0.46$). (e) Actual target boundary overlayed on OB-CSI final estimation. —— Actual target boundary; – – – Estimated target boundary; · · · CE initial conditions.

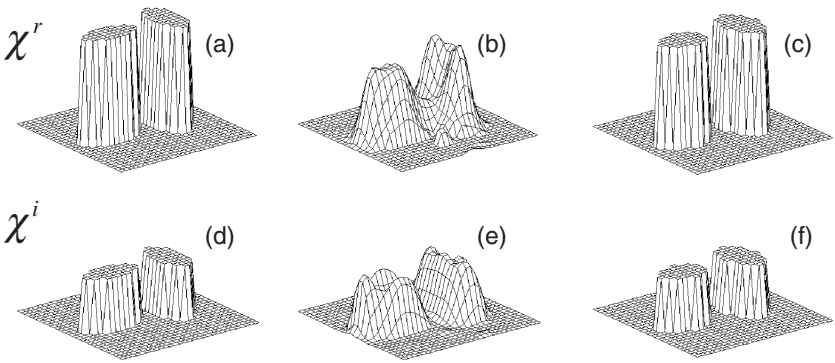

Figure 6. Double-target configuration (same contrast $\chi = 1 + i0.5$): reconstruction examples. Target 1: elliptic cylinder with center at $(x_{01}, z_{01}) = (-0.5\lambda_0, 0)$, radii $R_{x1} = 0.5\lambda_0$ and $R_{z1} = 0.25\lambda_0$. Target 2: elliptic cylinder with center at $(x_{02}, z_{02}) = (0.5\lambda_0, 0)$, radii $R_{x2} = 0.25\lambda_0$ and $R_{z2} = 0.5\lambda_0$. Other parameters are as in Figure 3. (a), (d) Ground truth (real and imaginary contrast, respectively). (b), (e) Pixel-based CSI initial estimate (subsection 3.2.3) after $M = 240$ iterations with $N_I = 10$ and $\beta = 10^{-4}$. (c), (f) Final OB-CSI reconstruction via two iterations of the algorithm in subsection 3.2. CE parameters: 250 τ-steps with $\gamma = 0.03$ plus 100 steps with $\gamma = 0.025$ (1st iteration), 150 steps with $\gamma = 0.025$ (second iteration); estimated contrast: $\hat{\chi} = 0.97 + i0.50$.

with contrast $\chi = 1 + i0.5$, and all other simulation parameters as in Figures 3 and 4. Reconstruction results are shown in Figures 6 and 7. Again, good accuracy in both target boundary (see Figure 7) and contrast estimation

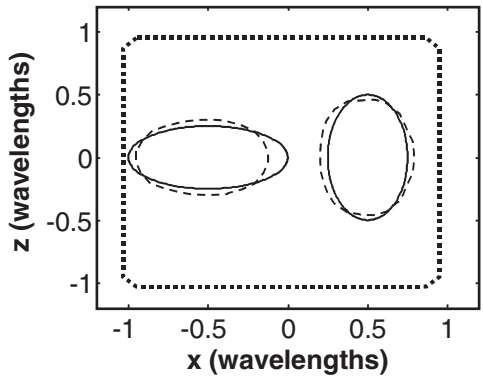

Figure 7. Parameters as in Figure 6. Actual target boundaries overlayed on OB-CSI final estimations. —— Actual target boundaries; – – – Estimated target boundaries; · · · CE initial conditions.

($\hat{\chi} = 0.97 + i0.50$) is observed. We emphasize that, despite the small separation between the two targets (a fraction of a wavelength), the proposed approach is remarkably capable to resolve them. Finally, we consider the case of a double-target configuration with *different* contrasts, namely,

- Target 1: Elliptic cylinder centered at $(x_{01}, z_{01}) = (-0.5\lambda_0, 0)$ with radii: $R_{x1} = 0.4\lambda_0$, $R_{z1} = 0.25\lambda_0$, and contrast $\chi_1 = 1 + i0.3$;
- Target 2: Elliptic cylinder centered at $(x_{02}, z_{02}) = (0.5\lambda_0, 0)$ with radii: $R_{x2} = 0.25\lambda_0$, $R_{z2} = 0.4\lambda_0$, and contrast $\chi_2 = 0.5 + i0.5$.

For this configuration, we used the following CE parameterization (generalizing (16))

$$\chi(\mathbf{r}) = \hat{\chi}_1 \Pi_{\mathscr{B}_1}(\mathbf{r}) + \hat{\chi}_2 \Pi_{\mathscr{B}_2}(\mathbf{r}) \tag{35}$$

with $\mathscr{B}_1$ and $\mathscr{B}_2$ denoting the (unknown) target domains, $\hat{\chi}_1$ and $\hat{\chi}_2$ indicating the corresponding (unknown) contrasts, and with the function $\Pi_{\mathscr{B}}$ defined in (17). The reconstruction algorithm, though slightly more involved, is formally analogous to that described in subsection 3.2. Results are shown in Figures 8 and 9. Reconstruction accuracy is comparable with those achieved in the previous examples.

As a general comment, in our numerical experiments, the range of applicability and the computational burden of the algorithm were found to be comparable with those in [6]. Our method should be viewed as an alternative CSI implementation featuring enhanced edge-preserving capabilities.

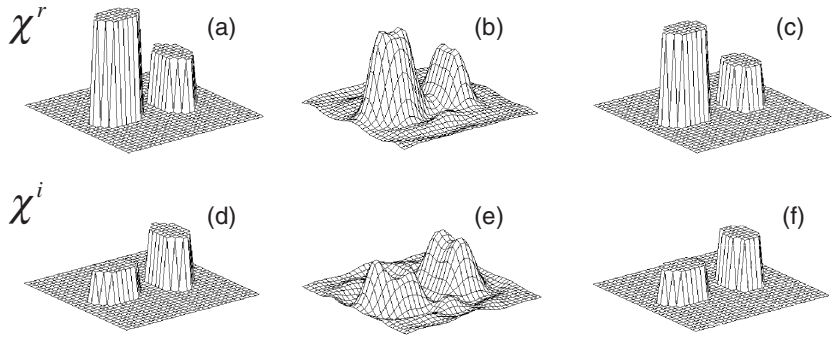

Figure 8. Double-target configuration (different contrasts): reconstruction examples. Target 1: elliptic cylinder with center at $(x_{01}, z_{01}) = (-0.5\lambda_0, 0)$, radii $R_{x1} = 0.4\lambda_0$ and $R_{z1} = 0.25\lambda_0$, and contrast $\chi_1 = 1 + i0.3$. Target 2: elliptic cylinder with center at $(x_{02}, z_{02}) = (0.5\lambda_0, 0)$, radii $R_{x2} = 0.25\lambda_0$ and $R_{z2} = 0.4\lambda_0$, and contrast $\chi_2 = 0.5 + i0.5$. Other parameters are as in Figure 3. (a), (d) Ground truth (real and imaginary contrast, respectively). (b), (e) Pixel-based CSI initial estimate (subsection 3.2.3) after $M = 240$ iterations with $N_I = 10$ and $\beta = 10^{-4}$. (c), (f) Final OB-CSI reconstruction via two iterations of the algorithm in subsection 3.2. CE parameters: 200 τ-steps with $\gamma = 0.04$ plus 150 steps with $\gamma = 0.025$ (1st iteration), 150 steps with $\gamma = 0.035$ (second iteration); estimated contrasts: $\hat{\chi}_1 = 0.89 + i0.27$, $\hat{\chi}_2 = 0.44 + i0.50$.

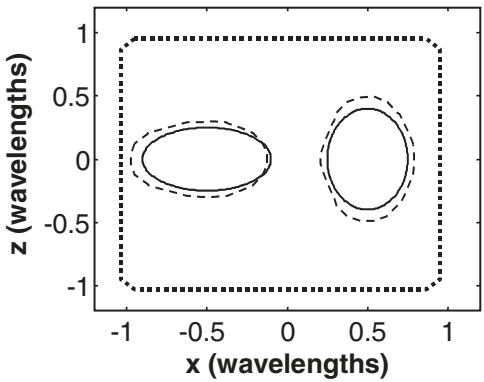

Figure 9. Parameters as in Figure 8. Actual target boundaries overlayed on OB-CSI final estimations. —— Actual target boundaries; – – – Estimated target boundaries; · · · CE initial conditions.

5. Conclusions

An object-based contrast source inversion (CSI) method has been presented for imaging of homogeneous targets embedded in a homogeneous, lossless background. In the proposed approach, the CSI method in [6] is

combined with a curve-evolution reconstruction technique in an alternating-minimization iterative scheme. Preliminary outcomes, so far restricted to 2-D geometries and time-harmonic excitation, look encouraging. The proposed approach should be viewed as an alternative implementation of the CSI method in [6], particularly suited for applications in which edge information is crucial. Applications to subsurface targets and full 3-D scenarios are under consideration. The case of *pulsed* excitation could be handled too, in principle, using the time-domain CSI approach in [44].

Acknowledgements

This work was supported by ODDR&E under MURI Grants ARO DAAG55-97-1-0013 and AFOSR F49620-96-1-0028, and by the Engineering Research Centers Program of the National Science Foundation under award number EEC-9986821. The work of V. Galdi was also supported by a European Union postdoctoral fellowship through the University of Sannio, Benevento, Italy.

References

1. Tikhonov, A.N. and Arsenin, V.Y., 1977, Solution of Ill-Posed Problems: V.H. Winston, Washington, D.C.
2. Bertero, M. and Pike, E.R. (eds.) 1992, Inverse Problems in Scattering and Imaging: Adam Hilger, Bristol.
3. Isernia, T., Pascazio, V., and Pierri, R., 2001, On the local minima in a tomographic imaging technique: IEEE Trans. Geosci. Remote Sensing, v. 39, no. 7, p. 1596–1607.
4. Colton, D. and Kress, R., 1992, Inverse Acoustic and Electromagnetic Scattering: Springer-Verlag, Berlin.
5. Bucci, O.M., Crocco, L., Isernia, T., and Pascazio, V., 2001, Subsurface inverse scattering problems: quantifying, qualifying, and achieving the available information: IEEE Trans. Geosci. Remote Sensing, v. 39, no. 11, p. 2527–2538.
6. van den Berg, P.M. and Kleinman, R.E., 1997, A contrast source inversion method: Inverse Problems, v. 13, p. 1607–1620.
7. Mumford, D. and Shah, J., 1989, Optimal approximations by piecewise smooth functions and associated variational problems: Communications on Pure and Applied Mathematics, v. 42, no. 4.
8. Tsai, A., Yezzi, T., and Willsky, A.S., 2001, Curve evolution implementation of the Mumford-Shah functional for image segmentation, denoising, interpolation and magnification: IEEE Transactions on Image Processing, v. 10, p. 1169–1186.
9. Vese, L. and Chan, T., 2002, A multiphase level set method for image segmentation using the Mumford and Shah Model: International Journal of Computer Vision, v. 50, p. 271–293.
10. Yezzi, A., Kichenassamy, S., Kumar, K., Olver, P., and Tennenbaum, A., 1997, A geometric snake model for segmentation of medical imagery: IEEE Trans. Medical Imaging, v. 16, no. 2, p. 199–209.
11. Shah, J., 2000, Riemannian drums, anisotropic curve evolution, and segmentation: J. Visual Comm. Image Representation, v. 11, no. 2, p. 142–153.

12. Chew, W.C., 1996, Waves and Fields in Inhomogeneous Media: Oxford Press, Oxford.
13. Abramowitz, M. and Stegun, I.A., 1964, Handbook of Mathematical Functions: Dover, New York.
14. Wang, Y. M. and Chew, W.C., 1989, An iterative solution of the two-dimensional inverse scattering problem: Int. J. Imaging System Technology, v. 1, p. 100–108.
15. Chew, W.C. and Wang, Y.M., 1990, Reconstruction of two-dimensional permitivity distribution using the distorted Born iterative method: IEEE Trans. Medical Imaging, v. 9, p. 218–225.
16. Habashy, T.M., Groom, R.W. and Spies, B., 1993, Beyond the Born and Rytov approximation: A nonlinear approach to electromagnetic scattering: J. Geophys. Res., v. 98, p. 1759–1775.
17. Devaney, A.J. and Sherman, G.C., 1982, Nonuniqueness in inverse source and scattering problems: IEEE Trans. Antennas Propagat., v. 30, p. 1034–1037.
18. Bojarski, N.N., 1982, Comments on 'Nonuniqueness in inverse source and scattering problems': IEEE Trans. Antennas Propagat., v. 30, p. 1037–1038.
19. Stone, W., 1982, Comments on 'Nonuniqueness in inverse source and scattering problems': IEEE Trans. Antennas Propagat., v. 30, p. 1037–1038.
20. Chew, W.C., Wang, Y.M., Otto, G., Lesselier, D., and Bolomey, J.C., 1994, On the inverse source method of solving inverse scattering problems: Inverse Problems, v. 10, no. 3, p. 547–553.
21. van den Berg, P.M. and Abubakar, A., 2001, Contrast source inversion method: State of art: J. Electromagnetic Waves Appls., v. 15, no. 11, p. 1503–1505.
22. Habashy, T.M., Oristaglio, M.L., and De Hoop, A.T., 1994, Simultaneous nonlinear reconstruction of two-dimensional permitivity and conductivity: Radio Science, v. 29, p. 1101–1108.
23. van den Berg, P.M. and Haak, K.F.I., 1997, Profile inversion by error reduction in the source type integral equations, in van den Berg, P.M., Block, H., and Fokkema, J.T. (eds.), Wavefields and Reciprocity: Delft University Press, p. 87–98.
24. Hansen, P.C., 1992, Analysis of discrete ill-posed problems by means of the L-curve: SIAM Review, v. 34, no. 4, p. 561–580.
25. van den Berg, P.M., van Broekhoven, A.L., and Abubakar, A., 1999, Extended contrast source inversion method: Inverse Problems, v. 15, p. 1325–1344.
26. Abubakar, A. and van den Berg, P.M., 2001, Total variation as a multiplicative constraint for solving inverse problems: IEEE Trans. Image Processing, v. 10, no. 9, p. 1384–1392.
27. Abubakar, A. and van den Berg, P.M., 2002, The contrast source inversion method for location and shape reconstructions: Inverse Problems, v. 18, no. 2, p. 495–510.
28. Chiu, C.-C. and Kiang, Y.-W., 1991, Inverse scattering of a buried conducting cylinder: Inverse Problems, v. 7, p. 187–202.
29. Budko, N.V. and van den Berg, P.M., 1998, Two-dimensional object characterization with an effective model: J. Electromagnetic Waves Appls., v. 12, p. 177–190.
30. Miller, E.L., Kilmer, M., and Rappaport, C., 2000, A new shape-based method for object localization and characterization from scattered field data: IEEE Trans. Geosci. Remote Sensing, v. 38, no. 4, p. 1682–1696.
31. Santosa, F., 1996, A level-set approach for inverse problems involving obstacles: SIAM: Control, Optimisation, and Calculus of Variations, v. 1, p. 17–33.
32. Litman, A., Lesselier, D., and Santosa, F., 1998, Reconstruction of a two-dimensional binary obstacle by controlled evolution of a level set: Inverse Problems, v. 14, p. 685–706.
33. Dorn, O., Miller, E.L., and Rappaport, C.M., 2000, A shape reconstruction method for electromagnetic tomography using adjoint fields and level sets: Inverse Problems, v. 16, p. 1119–1156.

34. Ramananjaona, C., Lambert, M., Lesselier, D., and Zolésio, J.-P., 2001, Shape reconstruction of buried obstacles by controlled evolution of a level set: From a min-max formulation to numerical experimentation: Inverse Problems, v. 17, p. 1087–1111.
35. Feng, H., 2002, Curve evolution object-based techniques for image reconstruction and segmentation, Ph.D. Dissertation, Boston University, Boston.
36. Feng, H., Karl, W.C., and Castañon, D.A., 2003, A curve evolution approach to object-based tomographic reconstruction: IEEE Trans. Image Processing, v. 12, no. 1, p. 44–57.
37. Galdi, V., Feng, H., Castañon, D.A., Karl, W.C., and Felsen, L.B., 2003, Moderately rough surface underground imaging via short-pulse quasi-ray Gaussian beams, to appear in IEEE Trans. Antennas and Propagat.
38. Galdi, V., Feng, H., Castañon, D.A., Karl, W.C., and Felsen, L.B., 2002, Multifrequency subsurface sensing in the presence of a moderately rough air-soil interface via quasi-ray Gaussian beams: Radio Science, Special Issue on 2001 URSI EMT Symposium.
39. Bertsekas, D.P., 1999, Nonlinear Programming: 2nd ed., Athena Scientific, Belmont, MA.
40. Press, W.H., Teukolsky, S.A., Vetterling, W.T., and Flannery, B.P., 1992, Numerical Recipes in C: The Art of Scientific Computing: 2nd ed., Cambridge Univ. Press, Cambridge, U.K.
41. Osher, S. and Sethian, J., 1988, Fronts propagation with curvature dependent speed: Algorithms based on Hamilton-Jacobi formulations: J. Comp. Physics, v. 56, p. 12–49.
42. Vogel, C.R. and Oman, M.E., 1998, Fast, robust total variation-based reconstruction of noisy, blurred images: IEEE Trans. Image Processing, v. 7, no. 6, p. 813–824.
43. Leviatan, Y. and Boag, A., 1987, Analysis of electromagnetic scattering from dielectric cylinders using a multifilament current model: IEEE Trans. Antennas and Propagat., v. 35, no. 10, p. 1119–1127.
44. Bloemenkamp, R.F. and van den Berg, P.M., 2000, Time-domain profile inversion using contrast sources: Inverse Problems, v. 16, no. 5, p. 1173–1193.